HARDWARE AND INSTRUMENTATION – Full Paper

Magnetic Resonance in Medicine 71:421–431 (2014)

Thermal Tissue Damage Model Analyzed for Different Whole-Body SAR and Scan Durations for Standard MR Body Coils

Manuel Murbach,[1,2]* Esra Neufeld,[1] Myles Capstick,[1] Wolfgang Kainz,[3] David O. Brunner,[2] Theodoros Samaras,[4] Klaas P. Pruessmann,[2] and Niels Kuster[1,5]

Purpose: This article investigates the safety of radiofrequency induced local thermal hotspots within a 1.5T body coil by assessing the transient local peak temperatures as a function of exposure level and local thermoregulation in four anatomical human models in different Z-positions.

Methods: To quantize the effective thermal stress of the tissues, the thermal dose model cumulative equivalent minutes at 43°C was employed, allowing the prediction of thermal tissue damage risk and the identification of potentially hazardous MR scan-scenarios. The numerical results were validated by B_1^+– and skin temperature measurements.

Results: At continuous 4 W/kg whole-body exposure, peak tissue temperatures of up to 42.8°C were computed for the thermoregulated model (60°C in nonregulated case). When applying cumulative equivalent minutes at 43°C damage thresholds of 15 min (muscle, skin, fat, and bone) and 2 min (other), possible tissue damage cannot be excluded after 25 min for the thermoregulated model (4 min in nonregulated).

Conclusion: The results are found to be consistent with the history of safe use in MR scanning, but not with current safety guidelines. For future safety concepts, we suggest to use thermal dose models instead of temperatures or SAR. Special safety concerns for patients with impaired thermoregulation (e.g., the elderly, diabetics) should be addressed. **Magn Reson Med 71:421–431, 2014. © 2013 Wiley Periodicals, Inc.**

Key words: local field enhancement; SAR; thermal dose; CEM43; safety

Magnetic resonance imaging (MRI) has established itself as a routine technique in medical diagnostics. The absence of ionizing radiation and the excellent soft-tissue contrast are major advantages of MR systems compared with computer tomography. Guidelines have been developed (1) to avoid potential patient risks due to (a) mechanical torque of metallic implants and acceleration of ferromagnetic objects, both by the static field, (b) nerve stimulation by the gradient fields, and (c) local tissue and whole-body heating by the radiofrequency fields. The history of safe use (2) indicates that quadrature-driven volume or body coils—as applied until today—are safe, when operated according to the guidelines.

In this article, we analyze the locally induced temperature rise as a function of scan time for different whole-body specific absorption rates (wbSAR) and different imaging positions. The estimated transient temperature increases are then translated into effective thermal load, applying the thermal dose model of cumulative equivalent minutes at 43°C (CEM43) (3). From literature values for maximum tolerable CEM43-doses (4), maximum allowed scan times before potential tissue damage occurs can be derived.

The CEM43 dose model expresses the thermal load on living tissues by estimating the equivalent induced thermal stress in minutes at 43°C. For example, exposing skin tissue for 16 min to 43°C (CEM43 = 16 min) causes equivalent symptoms as 64 min at 42°C, or 1 min at 47°C. Different tissues have different resiliences to thermal load. While skin may tolerate more than CEM43 = 40 min, more sensitive structures (e.g., blood brain barrier) show significant adverse effects already at CEM43 = 2 min.

In the current standard, absolute peak tissue temperatures are the governing limits, with maximum local tissue temperature of 40°C in the first level controlled operating mode (OM) according to (1). It is also stated that higher temperatures are accepted for specific tissues if no unacceptable risk for the patient occurs. However, there are no guidelines on how to control these limits. Only the wbSAR and partial-body SAR limits are provided, and these correlate poorly with localized exposure (e.g., peak spatial SAR averaged over any 10 g of tissue, psSAR10g) (5), and even less so with the local temperature increase, as shown in this study.

Assuming temperature independent dielectric parameters as a first approximation, the SAR distribution can be determined and translated to the induced temporal temperature distribution via a thermal simulation. Key parameters that determine local temperature increases are as follows: (a) the electromagnetic (EM) exposure level; (b) the spatial distribution of SAR, specific heat capacity,

[1]IT'IS Foundation, Zurich, Switzerland.

[2]Institute for Biomedical Engineering, University and ETH Zurich, Zurich, Switzerland.

[3]US Food and Drug Administration (FDA), Center for Devices and Radiological Health (CDRH), Silver Spring, Maryland, USA.

[4]Department of Physics, Aristotle University of Thessaloniki, Greece.

[5]Swiss Federal Institute of Technology (ETH), Zurich, Switzerland.

Grant sponsor: EUREKA; Grant number: E!4144; Grant sponsor: CTI; Grant number: 9193.1 (MRI+ Project).

*Correspondence to: Manuel Murbach, M.Sc., IT'IS Foundation, Zeughausstrasse 43, 8004 Zurich, Switzerland. E-mail: murbach@itis.ethz.ch

Received 6 July 2012; revised 19 December 2012; accepted 9 January 2013

DOI 10.1002/mrm.24671

Published online 14 February 2013 in Wiley Online Library (wileyonlinelibrary.com).

thermal conductivity, metabolic heat generation, and transient blood perfusion of the tissue; and (c) the thermal boundary conditions (convection, sweating, etc.).

RF induced temperature increases and local hotspots due to MR exposures were analyzed using anatomical models, for example, in (6–8). The strong temperature dependence of perfusion has been considered (6,9), but without employing a transient thermal dose model (CEM43). Various thermoregulatory effects exist, such as whole-body thermoregulation (10), redistribution of blood between body compartments and tissues (11) and local thermoregulation (12). The latter is particularly important with regard to local hotspots resulting from magnetic resonance imaging-induced heating (9).

Local SAR correlates poorly with temperature increase, even with temperature independent perfusion values, because of the vast tissue parameter inhomogeneities in the human body. Nonlinear local thermoregulation yields even weaker correlations. As the temperature weighted time-integrals correlate best with tissue damage, safety guidelines should be based on thermal dose models rather than local SAR or wbSAR limits. We, therefore, investigated the CEM43 dose concept (4) to estimate potentially hazardous combinations of exposure levels and MR scan setup configurations.

The overall goal of this study was to propose a novel safety approach for MR RF exposure assessment by:

- translating different MR RF exposure scenarios to transient temperature increases in realistic human models and various imaging positions
- considering the impact of local thermoregulation
- estimating cumulative equivalent minutes (CEM43) for different tissues in the transient heating process
- deriving maximum scan times before reaching tissue-specific thermal dose thresholds
- identifying potentially hazardous MR scan scenarios and comparing those with the history of safe use
- validating the simulation models with B_1^+ and skin-temperature measurements in one healthy subject

METHODS

Anatomical Models and Simulation Scenario

The evaluation was based on four different anatomical human models: Fats (m, 37 y, 1.81 m, and 120 kg) representing an obese male; Duke (m, 34 y, 1.78 m, and 76 kg), an average sized adult male; Ella (f, 26 y, 1.63 m, and 59 kg) an anatomically smaller female model; and Billie (f, 11 y, 1.45 m, and 35.6 kg), a child. They were positioned in 10 different Z-axis landmarks to identify the worst-case exposure scenario. The selected models of the Virtual Population [(13), www.itis.ethz.com/vip] are based on image data with a resolution better than $0.9 \times 0.9 \times 2$ mm^3, and consist of more than 69 different organs and tissues, which have been reconstructed as triangular surface meshes allowing for flexible discretization. The models and their positioning are depicted in Fig. 1, together with the generic 1.5 T birdcage models. The first model is the conservative birdcage with respect to B_1 excitation as defined in the ISO/TS10974 (14; high-pass, leg feed, 16 rungs with 16 current sources, 750 mm diameter, 650 mm length, tuned to 64 MHz circular polarization). The second birdcage is 400 mm long representing a shorter, more realistic birdcage. The simulation scenarios are as described in (5).

Tissue Properties and Local Thermoregulation

The dielectric and basal thermal tissue properties (including the metabolic heat generation rate) were assigned according to the comprehensive literature review of Hasgall (www.itis.ethz.ch/database), the recommended dielectric properties of which are largely identical to those proposed in (15). All digestive lumina were modeled as filled with air (5).

Thermal boundary conditions for systemic thermoregulation (sweating and breathing) are discussed later in the thermal simulation section. Accurate modeling of the local thermoregulation in human is challenging, as many parameters have systemic thresholds and interactions (e.g., sweating onset; increases in blood perfusion, metabolic rates, and cardiac output), which are also dependent on the extent of heat administration. Delayed temporal responses, thermal memories, and large intersubject variations further complicate predictions.

For local hotspots above 20 W/kg psSAR10g, thermoregulated local perfusion is the most important parameter for RF induced temperature increase (9), and is also the major tissue response to hyperthermia (16). Experimental assessments in humans are rare and usually date back some decades. They generally show perfusion saturation above 43−45°C, but state different onset temperatures (34−42°C) and have some differences in basal perfusion values.

Entire forearm perfusion in 5 subjects showed an exponential 10-fold increase between 34 and 45°C (17) and an overall 10-fold increase in 6 subjects at an elevated core temperature of 38°C (18). The forearm skin blood flow is reported to increase about 15-fold between 37 and 45°C (16). Thermoregulated muscle blood flow in the thighs of more than 20 subjects has been assessed by measuring the Xe^{133} washout by X-ray (19), estimating a very steep 16-fold increase. Perfusion in fat is estimated to reach a 10-fold increase at 45°C to match an experimental study in 5 subjects (20). Clinical hyperthermia studies estimate even higher thermoregulation capabilities, with a 42-fold increase in skin and 17-fold increase in muscle, to match their numerous experimental results (>3000 clinical hyperthermia treatments; 21).

Most of the recent modeling studies may have underestimated thermoregulation by applying increase factors up to 4 only [summarized in (9)], while Laakso and Hirata (9) argues for a 32-fold (skin) and 15-fold (other tissues) perfusion increase, which starts directly at basal temperature.

Based on this data, we widely followed the suggested model of Laakso and Hirata (9), with two differences: (a) we applied thermoregulation to skin, muscle and fat only, as literature values are more abundant and peak temperatures exclusively occur within these three tissues; and (b) the increase depends on absolute temperatures (not on the

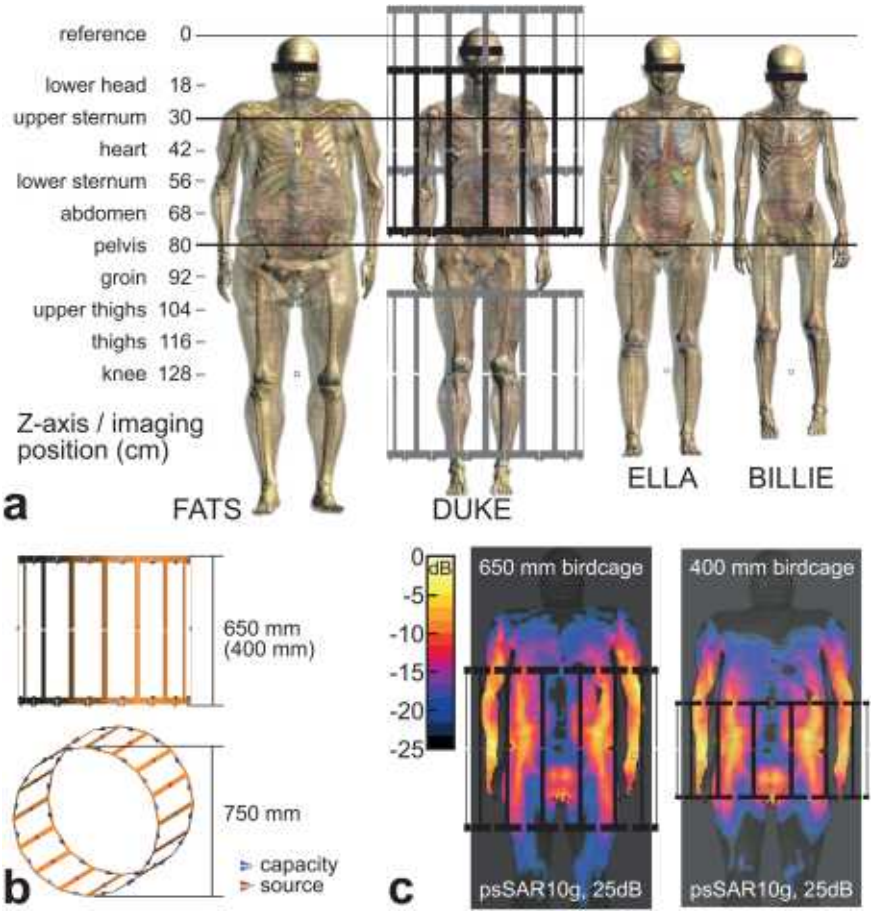

FIG. 1. **a**: The four anatomical models used in electromagnetic and thermal simulations and their positioning within the 1.5 T birdcage (assuming fixed model position and movement of the birdcage). Imaging positions are indicated. **b**: 16-Rung birdcage, 650 mm length used in general for the simulations, 400 mm for comparison. **c:** Illustrative SAR distribution for Fats in pelvis imaging position within the two birdcages. [Color figure can be viewed in the online issue, which is available at wileyonlinelibrary.com.]

local temperature increase), because our validation measurements in human skin did not support the assumption of significant perfusion increase below 37°C.

Thus, compared to Laakso, our thermoregulation model is less aggressive for tissues with basal temperatures below 37°C (mainly skin) and does not include other tissues. It models an exponentially temperature dependent increase factor of 32 for skin (from 37 to 45°C), and a factor of 15 for muscle and fat (from 37 to 43.3°C). The blood flow can be expressed as [similar to (9)].

$$\begin{aligned} B(T) &= B_0 \cdot L_b(T) \\ L_b(T) &= 1, \qquad T < 37^\circ C \\ L_b(T) &= 2^{\frac{T-37}{\Delta B}}, \qquad T \geq 37^\circ C \\ \max(L_b) &= 32(\text{skin}), 15(\text{muslce}, \text{fat}) \end{aligned} \quad [1]$$

where $B(T)$ is the perfusion rate at temperature T, L_b(T) the local temperature dependent multiplier, B_0 is the basal perfusion at or below 37°C, and ΔB (the local vasodilation parameter) = 1.6 to match the desired temperature dependent perfusion increase. The thermoregulated perfusion model is visualized in Fig. 2. For all considerations, fat also includes subcutaneous adipose tissue.

Data analysis was performed for:

- constant (basal) perfusion (modeling a completely dysfunctional thermoregulation)
- muscle, skin, and fat thermoregulated (fully functional/normal)

Although thermoregulatory processes show typical response times in the order of 10 min, instantaneous regulation was implemented. This may result in a perfusion overestimation, especially within the first 10 min of heating (before full physiological response). Cardiac output increase is included in the local perfusion increase model. The impact of sweating, room temperature, and breathing is discussed in the next section. No other temperature related effects were considered, for example, (a) change of EM energy absorption-distribution due to thermoregulation dependent dielectric parameter, (b) increased perfusion in tissues other than muscle, skin, and fat due to the higher cardiac output, (c) stealing effect (11), or (d) behavioral thermoregulation, where the patient may tend to change posture when feeling excess heat.

EM and Thermal Simulation

Details of the EM simulations can be found in (5). All simulations were performed using the finite difference time domain method with a uniform and isotropic grid resolution of 2 mm.

The SAR distributions were used as input for the thermal simulations, which were conducted with SEMCAD X, V14.8 (jointly developed with SPEAG, Zurich,

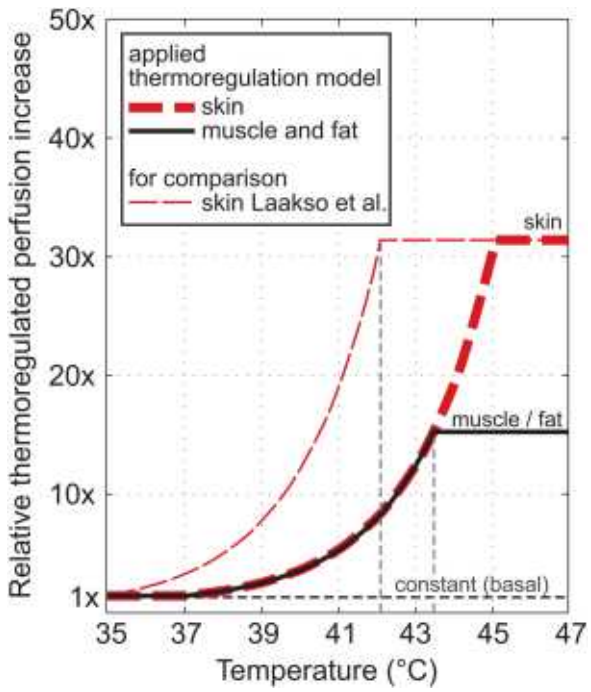

FIG. 2. Applied temperature-dependent local blood perfusion model for skin, muscle and fat. The Laakso model starts regulating at basal temperature already (around 35°C for skin), while the applied model in this study depends on absolute temperatures. The absolute blood flow is 106–3392 mL/min/kg for skin, 39–585 mL/min/kg for muscle and 33–495 mL/min/kg in fat. [Color figure can be viewed in the online issue, which is available at wileyonlinelibrary.com.]

Switzerland), based on the extended Pennes Bioheat equation (PBE, Eq. [2]):

$$\rho c \frac{\partial T}{\partial t} = \nabla \cdot (k(\vec{r}) \nabla T(\vec{r}, t)) + g(\vec{r}, t)$$
$$g(\vec{r}, t) = \rho Q + \rho S - \rho_b c_b \rho B (T - T_b) \quad [2]$$

where T is the temperature at location $\vec{r}$ and time t, c the specific heat capacity, k the thermal conductivity, ρ the density, B the perfusion rate, Q the metabolic heat generation rate, and S the spatial specific absorption rate (SAR). The index b indicates a property of blood.

The body-core-temperature was assumed to be fixed with a basal metabolic temperature (T_b) of 37°C, as its elevation is very small compared to local temperature increases (9). This was confirmed in the thermal validation measurement within this study, where 20 min with 3.6 W/kg wbSAR only induced a rectal core temperature rise of <0.3 K (compared with local skin temperature increases of almost 5 K), and is also in agreement with observations from hyperthermia (21), where core temperature is usually not exceeding 38°C, even for wbSAR values of up to 10 W/kg. However, small core temperature rises may still have a non-neglectable influence on thermal dose.

A Dirichlet thermal boundary condition was defined at major blood vessels and a convection dependent boundary condition at the interface to external and internal air ($h = 6$ and 10 W/m^2/K, respectively, $T_{Air} = 25$°C), which corresponds to normal breathing and normal clothing with little airflow (22). Air temperatures of up to 25°C are allowed by the standard without reducing the exposure level (1). Accurate modeling of the boundary condition is challenging, as part of the patient is lying on a soft table. However, while the boundary to air plays the major role for overall systemic heat dissipation, it has only marginal influence on the local internal peak temperatures. In addition, as the core temperature was fixed in this study, these boundary conditions had no influence on systemic heat dissipation in the simulations. To confirm these assumptions, the worst-case exposure scenario with Fats was simulated with very aggressive air-cooling (60 W/m^2/K convection coefficient, additional 600 W/m^2 constant heat flux from sweating, and $T_{Air} = 18$°C), corresponding to heavy sweating, fast airflow, and increased breathing rate (23). While the superficial 10 mm tissue layers showed significant temperature decreases (skin surface average from about 35 to 31°C), the extremity hotspots in the wrist and the inner hotspot near the pelvic bone were not influenced. In reality (non apriori-fixed core temperature), the sweating rate is adjusted to help maintaining a stable core temperature.

The applied PBE model (Eq. [2]) does not consider certain aspects, such as the variation of local blood temperature, the discreteness of vasculature and mass transport within vessels or the varying body-core-temperature. A time step of 2.6 s was chosen to maintain numerical stability in the 2 mm thermal simulation grid (CFL condition for stability). Conformal corrections were used to correct the overestimation of surface heat flux (staircasing effect) in the voxelled finite difference time domain model (24). As the thermoregulated perfusion models create nonlinear temperature increases, values could not be scaled with SAR (i.e., the thermoregulated model requires an individual simulation for each SAR exposure level). The explicit time-domain solver was configured with a lead-time of 30 min (without heating) to reach the baseline steady-state temperature distribution before heating with the maximum allowed exposure level of the first level controlled OM according to (1). The transient heating reached steady-state after about 20 min for the thermoregulated and 60 min for the constant perfusion model, which is in agreement with time scale observations from, for example, hyperthermia (25). The modeled instantaneous thermoregulation underestimates the transient temperatures during the heating phase, and overestimates temperatures in the cooling phase, whereas it has marginal influence on steady-state temperatures and reaching time. The cooling phase was not included in the thermal dose evaluations, as peak temperatures drop rapidly after switching off the RF exposure, such that thermal dose (CEM43) does not increase significantly anymore.

Data Evaluation

The EM exposures were normalized to the maximal limit for the first level controlled OM, that is, wbSAR: 4 W/kg; head SAR: 3.2 W/kg; and partial-body SAR: 4–10 W/kg (1). The local peak temperature (pT) was evaluated for a single voxel, and averaged in volumes of 1 cm^3 (125 voxels) and 10 cm^3 (1250 voxels); thermal dose evaluations were conducted with pT, that is, exceeding the thermal

damage threshold for one tissue-voxel was considered as the limitation.

The pTs of all landmark positions (at steady-state) were separately evaluated for tissues with the greatest temperature increases (muscle, skin, and fat) and within four body regions (head, trunk, arms, and legs).

For the position with the highest relevant steady-state temperature (Fats, pelvis centered), the temperature histogram was extracted for different tissues, and the transient temperature profiles were evaluated and translated to thermal dose (CEM43) for Fats and Duke. Based on tissue damage thresholds, maximum scan times were derived for the two different blood perfusion models, basal (constant) and thermoregulated perfusion.

Thermal Doses (CEM43) and Damage Threshold Levels

Thermal doses were derived by integrating a temperature-weighted function over time. The most prominent dose model (3) uses cumulative equivalent minutes at 43°C (CEM43) to accumulate temperatures above 39°C and calculates dose-equivalent minutes at 43°C as follows:

$$\mathrm{CEM}\,43(t) = \int_{t_0}^{t_{\mathrm{final}}} R^{(43-T(t))}\mathrm{d}t \qquad [3]$$

where t_0 signifies the beginning and t_{final} the end of the heating period. $T(t)$ is the temperature of the tissue of interest at time t, and R is a constant equal to 0.5 for $T(t) > 43$°C, 0.25 for $39° < T(t) < 43$°C, and $R = 0$ for $T(t) < 39$°C.

For the tissues primarily heated during MR exposures, the reported thermal thresholds for significant tissue damage were found above 41 CEM43 for muscle, fat, and skin, and around CEM43 = 15 min for bone (4,26). In more sensitive structures, for example, the blood brain barrier in the central nervous system, significant adverse effects were observed at CEM43 = 2 min. Therefore, the following tissue specific CEM43 thresholds have been applied to derive maximum scan times before running into potential tissue damage:

a. CEM43 = 15 min, limit for muscle, fat, skin, and bone tissue.
b. CEM43 = 2 min, limit for all other tissues.

In our study, we used pT (single voxel) for $T(t)$. While thermal tissue damage in a few cubic millimeters may be of minor importance for the overall health of a patient, it should still be considered significant, as it could for example cause the loss of neurons when pT occurs at according locations (26).

Experimental Validation

In a first step, the EM simulations were validated. The simulated B_1^+ field map of Duke (head imaging position) was compared with an MR scanner B_1^+ measurement of the actual person the Duke model is based on. The B_1^+ flip-angle measurement scan was performed in a Philips Achieva 3T, resulting in the absolute B_1^+ distribution in the head (27). The simulation was conducted with a generic birdcage with dimensions similar to that of the Philips scanner (16-rung birdcage, 400 mm length). Field levels of the simulation were matched to the experiment by applying the same B_1 field around the head as measured with the H-field probe H3DV7 (SPEAG, Zurich, Switzerland), calibrated for the applied RF sequence.

In a second step, thermal validation measurements were performed within the 64 MHz body coil of the MITS1.5 system (ZMT, Zurich, Switzerland), providing excellent control and ease of access. The physical birdcage geometry was identical to that of the generic model used for all simulations. The upper sternum of another volunteer (32 y, male, healthy, 1.88 m) was positioned at the isocenter as the simulations identified anatomically well-defined hotspot positions at the shoulder in this imaging position. A circularly polarized RF field was applied, yielding B_1^+ values of 3.0 and 6.0 μT (assessed with the H-field probe H3DV7, SPEAG), exposing the volunteer with 0.9 and 3.6 W/kg wbSAR (two consecutive experiments with 60 min recovery time in between). The exposure level was derived from the birdcage power budget and verified by simulations given that Duke and the volunteer have similar anatomical dimensions: height 1.79 vs. 1.88 m; bmi 23.1 vs. 23.7 kg/m^2; shoulder length 50 vs. 48 cm; age 34 vs. 32 years.

Three highly accurate high-resistance temperature probes (T1V3Lab, SPEAG) were placed at estimated temperature hotspot regions on both shoulders (T1 and T2; see Results section) and in the rectum (T3). Placement uncertainty was about 20 mm. T1 (left shoulder) was thermally isolated with medical compresses, reducing the temperature gradient near the body surface.

The same scenario was simulated with Duke. The convection coefficients on the ambient-air to skin boundary around T1 and T2 were adjusted slightly to yield similar initial skin temperatures as in the measurement. Values for the T1 (isolated) and T2 (nonisolated) convection coefficients were 10 and 15 W/m^2/K, respectively, compared with 6 W/m^2/K in other simulations, and the background air temperature was 24°C. The thermoregulated perfusion model was applied. For comparison, the variations of the temperature profiles of 400 surface skin voxels (10 × 20 × 2, two surface layers) around the hotspot regions were evaluated. This corresponds to a skin area of 20 × 40 × 4 mm^3 (about 3.5 g of skin, 2 mm voxel size), accounting for the probe placement uncertainty.

RESULTS

Figure 3 shows the local peak temperatures for Duke and Fats in different landmark positions, normalized to first level controlled OM. The highest relevant temperatures are found in the pelvis imaging position ($Z = 80$ cm), with values up to 42.8°C for a nonimpaired temperature-dependent perfusion model and 60°C for dysfunctional thermoregulation. In leg imaging positions ($Z = 104$–128 cm), very high B_1^+ fields are theoretically allowed by the standard (>7 μT) before reaching the partial-body SAR limit, yielding high temperatures. However, none of the MR manufacturers is currently using such high fields in this landmark region, which does not imply that they may not consider this in future systems. The pelvis imaging position is therefore considered the relevant worst-case heating scenario. The upper sternum imaging

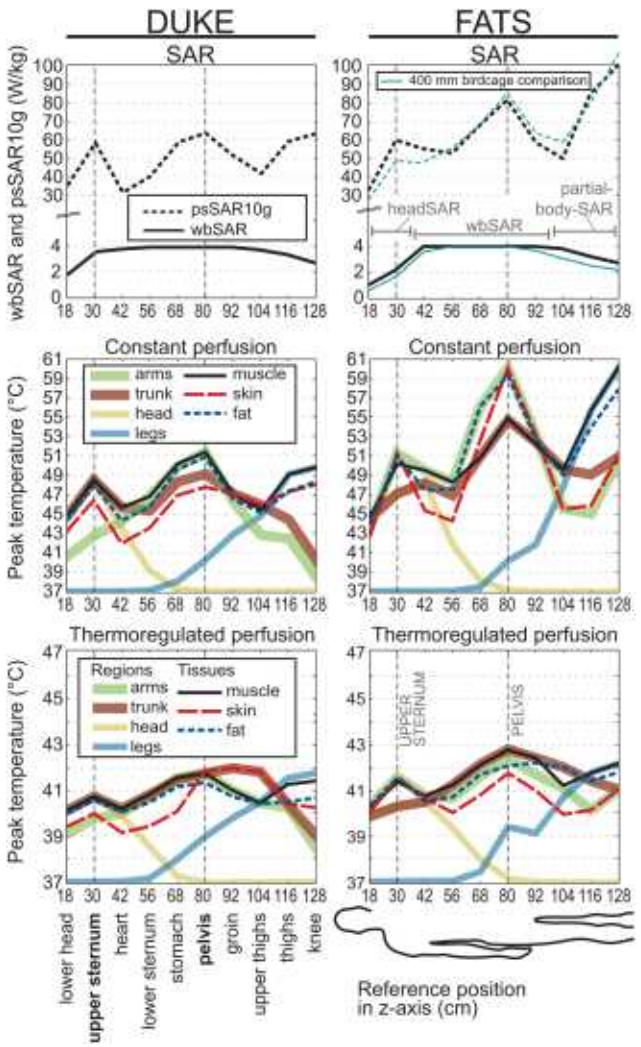

FIG. 3. psSAR10g, wbSAR, and steady-state peak temperatures (pT) as a function of landmark position for Duke and Fats and for different perfusion models. All exposures are normalized to first level controlled OM (the three different SAR limiting regimes are indicated). SAR values of the shorter 400 mm birdcage are shown for Fats for comparison. Evaluated tissue temperatures are plotted for four body regions and three tissues (hotspots occur exclusively in muscle, skin, or fat). Ella and Billie generally show lower temperature values (not depicted). [Color figure can be viewed in the online issue, which is available at wileyonlinelibrary.com.]

position was chosen for validation measurements. Ella and Duke show comparable psSAR10g values, but Ella has lower peak temperatures, as the psSAR10g in Ella is located in tissues with higher perfusion. Billie generally has lower values for psSAR10g and temperature (results of Ella and Billie are not depicted).

The short birdcage (Fig. 3) shows small deviations in SAR and temperature (latter not depicted). Highly exposed regions have very similar absorption patterns (Fig. 1). The psSAR10g values differ by <20% in Fats, peak Temperatures by <1 K (constant perfusion) and 0.4 K (thermoregulated). Due to the more localized exposure of the short birdcage, the partial-body SAR limit is reached earlier, such that 4 W/kg wbSAR can only be applied in centered torso positions.

Thermal hotspots occur exclusively in muscle, fat, and skin. The temperature distribution at steady-state across different tissues and regions of interest for the worst-case position in Fats (pelvis imaging position) is shown in Fig. 4. Although bones have lower SAR values, they show high temperature increases because of their low perfusion and proximity to strongly heated tissues. The central nervous system (including the spinal cord) and all other tissues have significantly lower peak temperatures.

Figure 5a illustrates the heating process in the time-domain and the pT of different tissues for the pelvis imaging position of Fats. These transient peak temperatures are accumulated (CEM43) for heating with different wbSAR levels, and the wbSAR is plotted against the scan time of reaching the tissue damage threshold limits (Fig. 5b,c). When applying tissue specific thresholds for Fats (Fig. 5b), muscle tissue first reaches its damage threshold (CEM43 = 15 min) after 25 min continuous exposure with 4 W/kg wbSAR in the thermoregulated case (indicated with red circles), indicating that muscle would be the most vulnerable tissue according to this approach. At constant perfusion, the threshold limit is reached first by skin tissues, after 4 min. In Duke (Fig. 5c), the threshold values are reached after 55 min for the thermoregulated model (after 10 min in the nonregulated case). Values for the other models are summarized in Table 1. Curves of the thermoregulated model were interpolated, as their nonlinear temperature increases cannot be scaled with wbSAR.

The B_1^+ field distribution derived from the simulation shows good qualitative correspondence to the relative MR flip-angle measurements (Fig. 6). A statistical comparison, however, is challenging because of the errors due to the

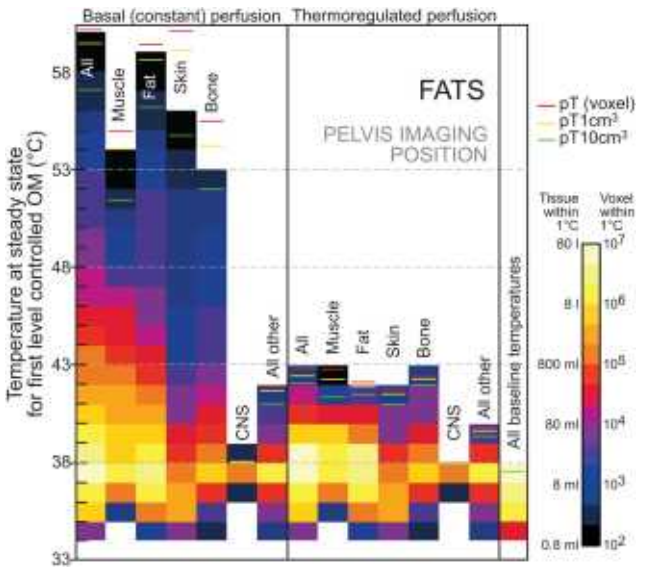

FIG. 4. Histographic view of the temperature distribution across highly exposed and other tissues of interest for Fats in the pelvis landmark position, wbSAR = 4 W/kg (first level controlled OM) and for constant as well as thermoregulated perfusion. Voxel peak temperature (pT), pT1cm^3, and pT10cm^3 are indicated. Central nervous system includes the spinal cord. The baseline temperatures are shown as well (thermal equilibrium before heating onset). [Color figure can be viewed in the online issue, which is available at wileyonlinelibrary.com.]

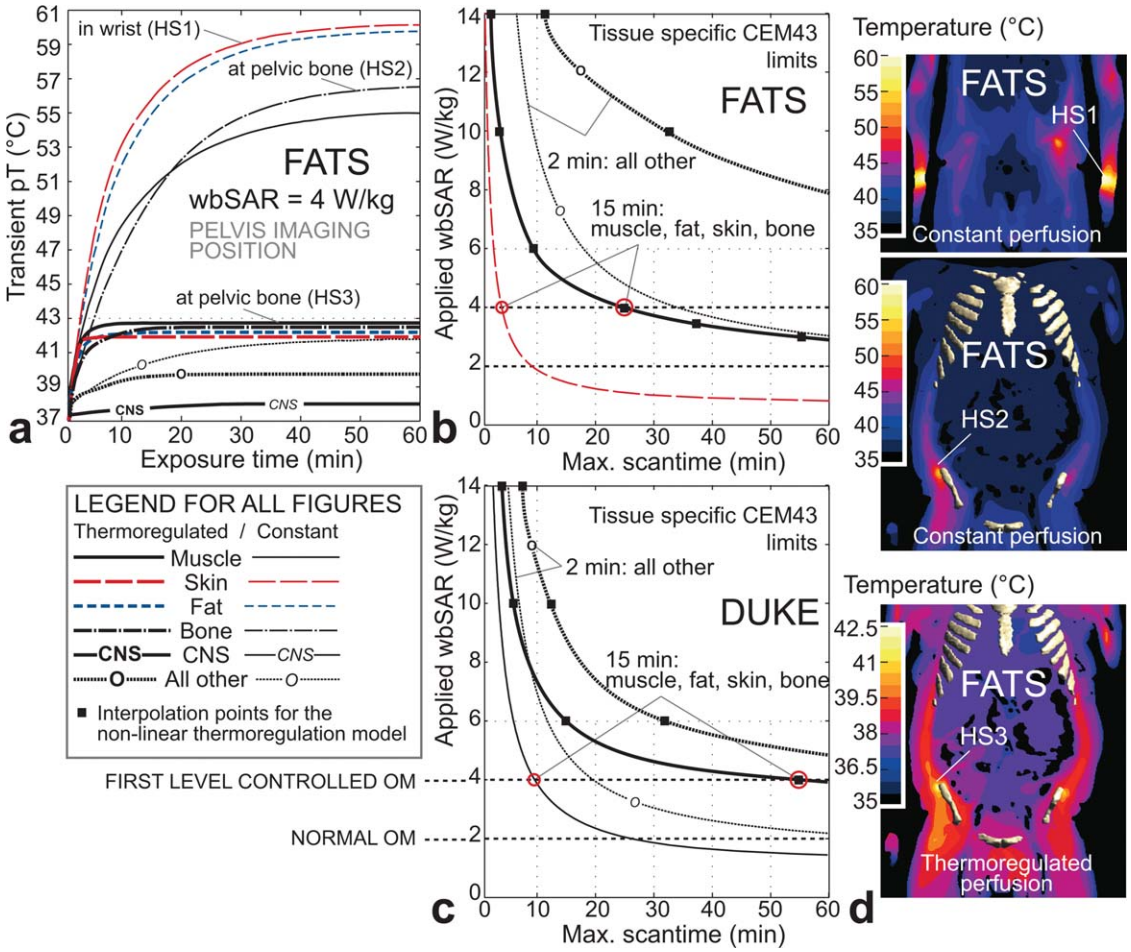

FIG. 5. **a**: Transient peak temperature during MR exposure of Fats (all figures are in pelvis imaging position). **b**: Scan times for Fats to reach the tissue specific CEM43 limits in the context of applied wbSAR exposure levels (at 4 W/kg: muscle tissue first reaches its limit in the thermoregulated case, skin for the constant perfusion; indicated with red circles). **c**: Corresponding scan times for Duke. **d**: Temperature distribution in coronal slices showing the different hotspot (HS) locations in Fats (different scales for constant and thermoregulated perfusion.

coarse measurement grid and various small-scale anatomical structures. In the visualized extraction lines, the B_1^+ field deviation is less than the combined expanded ($k=2$) uncertainty of 2 dB (~24%, field amplitude).

The thermal validation measurements and the corresponding simulations are within the combined expanded ($k=2$) uncertainty of 3.2 dB (~22%), thus supporting the assumption of high temperature induced perfusion changes, especially when comparing the performance of the thermoregulated model against the constant model (Fig. 7). The thermoregulation model according to Laakso would underestimate the peak temperatures in our measurement, as the thermoregulation in skin would start at the basal temperature already. The temperature profiles of the 400 skin voxels were characterized by their mean value, and 65% confidence interval (SD, $k=1$). The deviation of T2 in Fig. 7b exceeded one SD, which may result from differences in (a) positioning and (b) posture of the volunteer, (c) baseline perfusion in the low-dose experiment, (d) boundary conditions, and (e) anatomical

Table 1
Allowed Scan Times and Corresponding psSAR10g Values for Reaching Tissue Specific CEM43 Thresholds

Pelvis centered	First level OM (4 W/kg wbSAR)			Realistic OM (3 W/kg wbSAR)	Normal OM (2 W/kg wbSAR)	
Model	Regulated	Constant	psSAR10g	Regulated	Regulated	Constant
Fats (120 kg)	25 min	4 min	81 W/kg	56 min	140 min	9 min
Duke (76 kg)	55 min	10 min	62 W/kg	170 min	402 min	26 min
Ella (59 kg)	106 min	11 min	65 W/kg	233 min	> 600 min	28 min
Billie (35 kg)	290 min	16 min	46 W/kg	560 min	> 600 min	62 min

wbSAR (3 W/kg) is assumed to be a realistic maximum exposure in first level controlled OM (averaged over 1 h), when considering the manufacturer's safety margin and frequent interruptions between sequences.

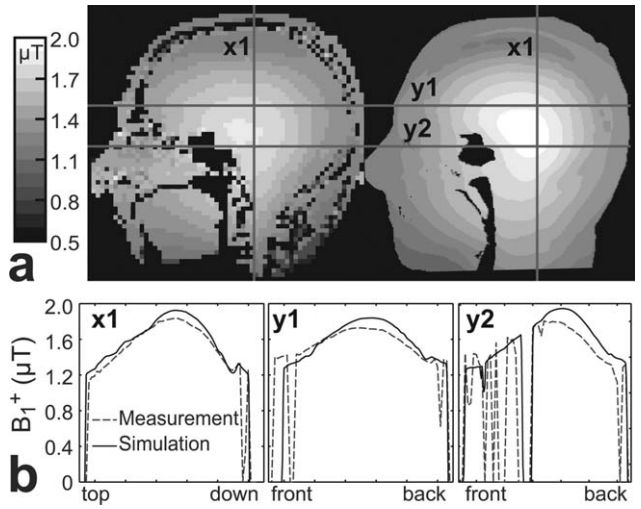

FIG. 6. B_1^+ simulation and measurement of Duke and the actual person the Duke model is based on. **a**: Sagittal view of the simulated (left) and measured (right) B_1^+ field (0.1 μT per contour) and (**b**) three extraction lines (x1, y1, and y2) are shown for comparison.

structure. Figure 7c shows the delayed thermoregulatory perfusion change, where the measured temperature suddenly stops increasing after 10 min (it even slightly decreases). The perfusion in the first 10 min is overestimated in the simulation because of the implemented immediate thermoregulation model.

Numerical Uncertainty

The numerical and measurement uncertainty analysis (Table 2) was based on the concept of NIST TN1297 (28). The thermoregulated temperature increase model and maximum scan time derivation is highly nonlinear. The corresponding uncertainty assessment was performed only for the worst-case positioning (pelvis) with the Fats model, and cannot be used for other positions, models, or exposure levels.

The influence on our obtained results, that is, peak temperature and derived maximum scan time, was determined based on the modeling parameter uncertainties from (a) the underlying EM simulation and (b) the thermal simulation (Table 2).

The combined root sum squared uncertainty (RSS, single standard deviations, $k=1$) is estimated to be 0.51 dB (~12%) for the local SAR enhancement (psSAR10g normalized to wbSAR) and 1.28 dB (~30%) for peak temperature increase with constant perfusion [both in agreement with (29), i.e., 11 and 31%]. The uncertainty for peak temperature increase in the thermoregulated case is lower (0.9 dB, ~21%), as the modeled perfusion increase suppresses the variation (nonlinear suppression).

As the CEM43 dose accumulation increases by factor 4 with each additional degree Celsius above 39°C (factor 2 above 43°C, Eq. [3]), uncertainty for thermal dose is non linear for both perfusion models. The derived maximum scan times before reaching the dose limit have estimated uncertainty values of 1.2 dB (~27%, constant perfusion) and 2.1 dB (~50%, thermoregulated). The measurement uncertainties for B_1^+ and temperature are 0.9 and 1.4 dB, respectively (see Table 2c,d).

DISCUSSION AND CONCLUSIONS

Temperature-regulated perfusion significantly lowers the maximum temperature increase compared to static perfusion values. At the first level controlled OM, it is about a factor 3–4 (from 8–23 K down to 3–6 K) depending on

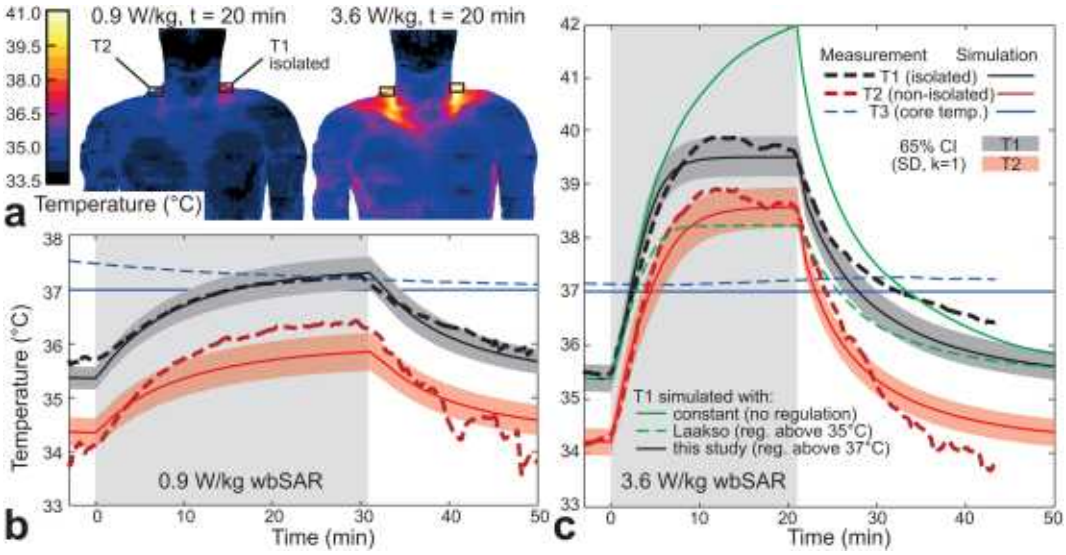

FIG. 7. **a**: Numerical prediction of hotspot locations in Duke, (**b**) low- and, (**c**) high-dose experiment showing skin surface temperature measurements near the predicted temperature hotspots on the shoulder (T1 thermally isolated, T2 nonisolated) and simulation of the same scenario using the thermoregulation model. The simulation curves are the mean of 400 surface skin voxels and their 65% confidence interval (CI). This estimates the probe placement uncertainty (20 mm) at the high temperature gradient around the hotspot. Core temperature remained stable during the experiments. Thermoregulation starts above 37°C, except for the Laakso model. Constant perfusion and the Laakso thermoregulation model show considerable deviation to our measurement results in skin. [Color figure can be viewed in the online issue, which is available at wileyonlinelibrary.com.]

Table 2
Standard Combined Uncertainties for (a,b) the Numerical Evaluations (Fats in Pelvis Position), (c) the B1+ Assessment, and (d) Thermal Measurements (Duke/Volunteer in Upper Sternum Position)

Parameter	Range	u_i	
(a) EM Simulation		psSAR10g per wbSAR[a]	
Convergence	Simulation length: +100%	0.03 dB	
Model discretization	Voxel size: 0.5 mm, 3 mm	0.26 dB	
Dielectric parameter	σ: ±10%	0.05 dB	
Dielectric parameter	ε: ±10%	0.17 dB	
Dielectric contrast	σ: ±10%, in single tissue	0.09 dB	
Dielectric contrast	ε: ±10%, in single tissue	0.08 dB	
Density contrast	ρ: ±10%, in single tissue	0.26 dB	
Anatomical model accuracy	According to (29)	0.28 dB	
RSS: Local SAR uncertainty		0.51 dB (−11%; +12%)	
(b) Thermal Simulation (worst case scenario, steady-state)		pT, Thermoregulated	pT, Constant perf.
Local SAR uncertainty	from (a)	0.40 dB[b]	0.40 dB
Convergence	Simulation length and time step	0.04 dB[b]	0.05 dB
Model discretization	Voxel size: 0.5 mm, 3 mm	0.19 dB[b]	0.26 dB
Thermal parameter	c: ± 10%	0.00 dB[b]	0.00 dB
Thermal parameter	k: ± 20%	0.05 dB[b]	0.26 dB
Thermal parameter	Q: ± 20%	0.08 dB[b]	0.02 dB
Blood heat capacity	$\rho_b \cdot c_{b:}$ ± 10%	0.16 dB[b]	0.16 dB
Thermal boundary cond.	h: ± 50%	0.12 dB[b]	0.11 dB
Basal (constant) perfusion	B_0: ± 50% (all tissues)	0.26 dB[b]	1.14 dB
Perfusion increase	L_b: ± 50%	0.70 dB[b]	n.a.
RSS: Peak temperature increase uncertainty, actual estimated value and resulting uncertainty interval in peak temperature		0.90 dB[b], 42.8°C (41.7°; 44.1°)	1.28 dB, 60°C (54.1°; 67.9°)
Corresponding max. scan time uncertainty (in defined worst-case scenario for CEM43 = 15 min limit), actual estimated value and uncertainty interval		2.1 dB[b], 25 min (16 min; 41 min)	1.2 dB[b], 4 min (3 min; 5.3 min)
(c) B1+ validation measurement			
Assessment of relative B1+ map (27)		0.6 dB	
B-field probe uncertainty for reference B1+ measurement		0.6 dB	
Age induced changes [6 years between model segmentation and B1+ mapping, from (29)]		0.3 dB	
Head positioning in scanner		0.1 dB	RSS (*a*) + (*c*):
RSS: B1+ measurement uncertainty		0.9 dB (−18%; +22%)	1.0 dB (k = 1); 2.0 dB (k = 2)
(d) Temperature increase validation measurement (assessment for T1 at high dose experiment)			
Temperature probe uncertainty		< 0.1 dB	
Incidence B1 field assessment		0.6 dB	
Probe placement (20 mm)		1.0 dB	
Probe thermal contact		0.5 dB	
Volunteer positioning (100 mm)		0.3 dB	
Differences between Duke and the actual volunteer		0.3 dB	
Thermal equilibration		0.5 dB	RSS (*b*) + (*d*):
RSS: Thermal validation measurement uncertainty, actual estimated value and uncertainty interval		1.4 dB, 39.5°C (38.8°; 40.5°)	1.6 dB (k = 1); 3.2 dB (k = 2)

[a]Relative local SAR uncertainty, as exposure is normalized to wbSAR.
[b]Highly nonlinear model. Values only valid for this specific worst-case (Fats, pelvis position, and first level OM).
Stated uncertainty values are standard deviations (k = 1) in the assumed log-normal probability distribution. Since they are uncorrelated, they can be combined by root-sum-square (RSS) procedures.

the model and position (Fig. 3). The thermoregulated perfusion is therefore the most influential parameter for local temperature increase and related damage for the given exposure scenarios. Other factors, such as sweating, airflow, or room temperature, result in altered skin temperatures but have little influence on local internal peak temperatures.

Body core temperature is considered fixed at 37°C, which was confirmed by the validation measurement and experience in hyperthermia, and thus has a minor influence on local temperatures. The peak temperature increases in hyperthermia are similar for comparable SAR levels, but a direct comparison is difficult due to the intrinsic difference of exposure, that is, focused absorption versus B_1^+ homogeneity optimization.

In summary, the maximum scan times of Table 1 (partially derived from Fig. 5) have been estimated in the identified worst-case position (pelvis imaging) for the

investigated models. The Fats model reaches the damage threshold limits first in all configurations. At first glance, the history of safe use of whole-body MR coils seems to contradict the presented thermal dose estimations as the current safety guidelines accept exposures in the first level controlled OM for 60 min (1). However, actual clinical use shows that:

- The IEC standard is very rarely fully exploited:
  A. Exposure is frequently interrupted (different sequences), leading to lower average SAR.
  B. The vast majority of scans are believed to be shorter than 30 min.
  C. The manufacturers' safety margins lead to an effective wbSAR of presumably about ~2.7–3.7 W/kg instead of the allowed 4 W/kg.
- As most patients are awake during MR scans, they may provide direct feedback on excessive heat sensations to the operator. However, some tissues may have limited heat sensation [e.g., muscle (30)].
- The actual thermal tissue damage thresholds in human might actually be higher than the ones used for this study.
- The peak temperature is reached in only a few cubic millimeters of tissue (pT). The average temperature of the hottest 1 g of tissue is 0.5–1.0°C lower in the thermoregulated case ($pT1cm^3$; Fig. 4), which would corresponds to factor 2–4 longer acceptable scan times. It remains unclear whether exceeding damage thresholds in <1 g of tissue could be acceptable in some tissues.

Therefore, the results of this study may well correspond with the history of safe use. All investigated human models accept roughly 1 h exposure to a realistic average wbSAR of 3 W/kg (Table 1). However, the study also demonstrates that the guideline limit for local tissue temperatures [40°C, (1)] is exceeded in all positions for Fats and Duke in the first level controlled OM. Therefore, the current safety guidelines should be revised. A new concept could be based on the thermal dose model (CEM43) in conjunction with tissue-specific thresholds. Such an implementation may be challenging due to the complex thermal parameter space. Especially, the high sensitivity of CEM43 below 43°C causes systematic problems, where a difference of only 1°C leads to factor of 4 change in allowed scan times. Nevertheless, we believe that having a better surrogate for actual tissue damage with larger uncertainty may become more useful in the future than wbSAR and local SAR limitations, which have very limited correlation to tissue temperature and tissue damage. More research on local thermoregulatory and tissue damage processes is therefore of high importance. The investigated dose model also allows considering transient temperatures and tissue sensitivity.

The presented results indicate that the greatest health risk from MR RF exposure can arise from a combination of (a) high exposure levels (i.e., first level controlled OM), (b) long scan times, (c) anatomically large and obese patients, and (d) patients with disabled or partially dysfunctional perfusion abilities (e.g., the elderly, diabetics) or heat sensation [e.g., paraplegics, (31)]. As patients with impaired or dysfunctional thermoregulation abilities might require special considerations, it is important to derive sound tissue damage thresholds and better thermoregulation modeling capabilities, based on accurate perfusion rates for the entire patient population.

In clinical practice, a different type of tissue damage mechanism is currently observed. High, very locally induced electric fields can lead to immediate burns. In many of these cases, the limbs or other body parts of the patients were in direct contact with RF coils or skin-to-skin contact points and loops were suspected to be responsible for these injuries (32). Other investigations are needed to understand how to assess these burns due to high induced electric fields, where thermoregulation is absent due to their acute nature.

REFERENCES

1. International Electrotechnical Commission. International standard, Medical equipment–IEC 60601-2-33: particular requirements for the safety of Magnetic resonance equipment, 3rd edition; Geneva: IEC, 2010.
2. Marshall J, Martin T, Downie J, Malisza K. A comprehensive analysis of MRI research risks: in support of full disclosure. Can J Neurol Sci 2007;34:11–17.
3. Sapareto SA, Dewey WC. Thermal dose determination in cancer therapy. Int J Radiat Oncol Biol Phys 1984;10:787–800.
4. Yarmolenko PS, Moon EJ, Landon C, Manzoor A, Hochman DW, Viglianti BL, Dewhirst MW. Thresholds for thermal damage to normal tissues: an update. Int J Hyperthermia 2011;27:320–343.
5. Murbach M, Cabot E, Neufeld E, Gosselin M-C, Christ A, Kuster N. Local SAR enhancements in anatomically correct children and adult models as a function of position within 1.5 T MR body coil. Prog Biophys Mol Biol 2011;107:428–433.
6. Nadobny J, Szimtenings M, Diehl D, Stetter E, Brinker G, Wust P. Evaluation of MR-induced hot spots for different temporal SAR modes using a time-dependent temperature gradient treatment. IEEE Trans Biomed Eng 2007;54:1837–1850.
7. Wang Z, Lin JC, Mao W, Liu W, Smith MB, Collins CM. SAR and temperature: simulations and comparison to regulatory limits for MRI. J Magn Reson Imaging 2007;26:437–441.
8. Hand JW, Li Y, Hajnal J V. Numerical study of RF exposure and the resulting temperature rise in the foetus during a magnetic resonance procedure. Phys Med Biol 2010;55:913–930.
9. Laakso I, Hirata A. Dominant factors affecting temperature rise in simulations of human thermoregulation during RF exposure. Phys Med Biol 2011;56:7449–7471.
10. Fiala D, Lomas K, Stohrer M. A computer model of human thermoregulation for a wide range of environmental conditions: the passive system. J Appl Physiol 1999;87:1957.
11. Foster KR, Adair ER. Modeling thermal responses in human subjects following extended exposure to radiofrequency energy. Biomed Eng (Online) 2004;3:4.
12. Lang J, Erdmann B, Seebass M. Impact of nonlinear heat transfer on temperature control in regional hyperthermia. IEEE Trans Biomed Eng 1999;46:1129–1138.
13. Christ A, Kainz W, Hahn EG, et al. The Virtual Family—development of surface-based anatomical models of two adults and two children for dosimetric simulations. Phys Med Biol 2010;55:N23–38.
14. International Standardization Organisation, ISO/TS 10974:2012, Requirements for the safety of magnetic resonance imaging for patients with an active implantable medical device. Geneva: ISO, 2012.
15. Gabriel S, Lau R, Gabriel C. The dielectric properties of biological tissues: II. Measurements in the frequency range 10 Hz to 20 GHz. Phys Med Biol 1996;41:2251.
16. Stolwijk JAJ. Mathematical models of thermal regulation. Ann N Y Acad Sci 1980;335:98–106.
17. Barcroft H, Edholm O. The effect of temperature on blood flow and deep temperature in the human forearm. J Physiol 1943;102:5–20.

18. Taylor WF, Johnson JM, O'Leary D, Park MK. Effect of high local temperature on reflex cutaneous vasodilation Effect of high local temperature on reflex cutaneous vasodilation. J Appl Physiol 1984;57:191–196.
19. Emery AF, Sekins MK. The use of heat transfer principles in designing optimal diathermy and cancer treatment modalities. Int J Heat Mass Transfer 1982;25:823–834.
20. Franco W, Kothare A, Ronan SJ, Grekin RC, McCalmont TH. Hyperthermic injury to adipocyte cells by selective heating of subcutaneous fat with a novel radiofrequency device: feasibility studies. Lasers Surg Med 2010;42:361–370.
21. Wust P, Nadobny J, Szimtenings M, Stetter E, Gellermann J. Implications of clinical RF hyperthermia on protection limits in the RF range. Health Phys 2007;92:565–573.
22. Bernardi P, Cavagnaro M, Pisa S, Piuzzi E. Specific absorption rate and temperature elevation in a subject exposed in the far-field of radio-frequency sources operating in the 10-900-MHz range. IEEE Trans Biomed Eng 2003;50:295–304.
23. Fiala D, Lomas KJ, Stohrer M. Computer prediction of human thermoregulatory and temperature responses to a wide range of environmental conditions. Int J Biometeorol 2001;45:143–159.
24. Neufeld E, Chavannes N, Samaras T, Kuster N. Novel conformal technique to reduce staircasing artifacts at material boundaries for FDTD modeling of the bioheat equation. Phys Med Biol 2007;52:4371–4381.
25. Wust P, Stahl H, Löffel J, Seebass M, Riess H, Felix R. Clinical, physiological and anatomical determinants for radiofrequency hyperthermia. Int J hyperthermia 2000;11:151–167.
26. Dewhirst MW, Viglianti BL, Lora-Michiels M, Hanson M, Hoopes PJ. Basic principles of thermal dosimetry and thermal thresholds for tissue damage from hyperthermia. Int J Hyperthermia 2003;19:267–294.
27. Brunner DO, Pruessmann KP. B1(+) interferometry for the calibration of RF transmitter arrays. Mag Reson Med 2009;61:1480–1488.
28. Taylor BN. KCE. Guidelines for evaluating and expressing the uncertainty of NIST measurement results. NIST Technical Note 1994;1297.
29. Bakker JF, Paulides MM, Neufeld E, Christ A, Kuster N, Van Rhoon GC. Children and adults exposed to electromagnetic fields at the ICNIRP reference levels: theoretical assessment of the induced peak temperature increase. Phys Med Biol 2011;56:4967–4989.
30. Graven-Nielsen T, Arendt-Nielsen L, Mense S. Thermosensitivity of muscle: high-intensity thermal stimulation of muscle tissue induces muscle pain in humans. J Physiol 2002;540:647–656.
31. Paprottka FJ, Machens H-G, Lohmeyer JA. Third-degree burn leading to partial foot amputation - Why a notebook is no laptop. J Plast Reconstr Aesthet Surg 2012;23:10–13.
32. Shellock FG, Crues J V. Radiology MR procedures: biologic effects, safety, and patient care. Radiology 2004;232:635–652.